Process Optimization for 100W Nanosecond Pulsed Fiber Laser Engraving of 316L Grade Stainless Steel

Journal of
Manufacturing and Materials Processing

MDPI

Article

Process Optimization for 100 W Nanosecond Pulsed Fiber Laser Engraving of 316L Grade Stainless Steel

Stephen D. Dondieu [1,*], Krystian L. Wlodarczyk [1,2], Paul Harrison [3], Adam Rosowski [3,4], Jack Gabzdyl [3], Robert L. Reuben [2] and Duncan P. Hand [1]

1 Institute of Photonics and Quantum Sciences, School of Engineering and Physical Sciences, Heriot-Watt University, Edinburgh EH14 4AS, UK; K.L.Wlodarczyk@hw.ac.uk (K.L.W.); D.P.Hand@hw.ac.uk (D.P.H.)
2 Institute of Mechanical, Process and Energy Engineering, School of Engineering and Physical Sciences, Heriot-Watt University, Edinburgh EH14 4AS, UK; R.Reuben@hw.ac.uk
3 SPI Lasers UK Ltd., 6 Wellington Park Tollbar Way, Hedge End, Southampton S030 2QU, UK; Paul.Harrison@spilasers.com (P.H.); Adam.Rosowski@spilasers.com (A.R.); Jack.Gabzdyl@spilasers.com (J.G.)
4 Institute for Manufacturing, University of Cambridge, 17 Charles Babbage Road, Cambridge CB3 0FS, UK
* Correspondence: sdd1@hw.ac.uk; Tel.: +44-(0)131-451-3084

Received: 9 November 2020; Accepted: 24 November 2020; Published: 26 November 2020

Abstract: High average power (>50 W) nanosecond pulsed fiber lasers are now routinely available owing to the demand for high throughput laser applications. However, in some applications, scale-up in average power has a detrimental effect on process quality due to laser-induced thermal accumulation in the workpiece. To understand the laser–material interactions in this power regime, and how best to optimize process performance and quality, we investigated the influence of laser parameters such as pulse duration, energy dose (i.e., total energy deposited per unit area), and pulse repetition frequency (PRF) on engraving 316L stainless steel. Two different laser beam scanning strategies, namely, sequential method (SM) and interlacing method (IM), were examined. For each set of parameters, the material removal rate (MRR) and average surface roughness (S_a) were measured using an Alicona 3D surface profilometer. A phenomenological model has been used to help identify the best combination of laser parameters for engraving. Specifically, this study has found that (i) the model serves as a quick way to streamline parameters for area engraving (ii) increasing the pulse duration and energy dose at certain PRF results in a high MRR, albeit with an associated increase in S_a, and (iii) the IM offers 84% reduction in surface roughness at a higher MRR compared to SM. Ultimately, high quality at high throughput engraving is demonstrated using optimized process parameters.

Keywords: nanosecond laser pulses; pulsed fiber lasers; engraving; high average power; surface roughness; material removal rate; interlacing method; sequential method

1. Introduction

The use of lasers for rapid prototyping of tools for injection molds, coin dies, stamps, and product identification through engraving has been an established process for some time [1–3]. High flexibility, lack of tool wear, ability to process a wide range of materials, high machining accuracy, and precision are some undeniable advantages in comparison to other engraving processes [4,5]. Both ultrashort pulsed (femtosecond and picosecond) and short-pulsed (nanosecond and microsecond) lasers can be used for engraving metals. These two classes of lasers differ fundamentally in the mechanisms of laser–material interaction and material removal during processing as extensively discussed elsewhere [6,7]. Generally, ultrashort pulsed lasers are noted for high-quality applications and high cost of purchase, maintenance,

and operation. Nanosecond lasers, on the other hand, are less costly and are well-established as process tools, making them much more popular and reliable for industrial applications.

Industry increasingly demands high manufacturing throughput to minimize costs, and this has propelled the commercial development of pulsed lasers with a higher average power. Master oscillator power amplifier (MOPA)-based nanosecond pulsed fiber lasers have become popular due to their high reliability and effective thermal management [8–10]. However, this scaling of power does not always lead to a concomitant increase in process speed and surface quality due to laser-induced thermal accumulation, the accumulation of structural defects, and particle shielding [11–14]. Over the years, much research effort has been expanded to remediate the effects of thermal build-up in the workpiece during high average power applications to make these lasers industrially acceptable. The research approach is generally to conduct a parametric survey to understand laser–material interactions and also investigate various laser processing strategies to mitigate the issues of thermal load [14–17].

So far, published research has been skewed towards ultrashort pulsed lasers, with relatively little literature on the potential of higher average power nanosecond pulsed lasers. This can be attributed to the general view that using nanosecond pulsed lasers with an average power greater than 50 W leads to an uncontrollable process [11]. Consequently, there is a current gap in the literature on the physical effects of higher average power nanosecond lasers on the material removal rate (MRR) and surface roughness (S_a). Again, although the use of the single-line machining experiments for investigating parametric influence during laser interactions is well established [11,18], the "scaling up" of findings from single lines to the more industrially relevant area engraving has not been reported. This scale-up introduces a further key parameter set, namely, the laser beam scanning strategy, including interlacing, which has been reported as an effective process route for the machining of borosilicate glass [19], and more complex scanning patterns, such as halftone printing angles, that have been shown to provide a good surface polishing effect [20].

This article extends the idea of IM for the engraving of 316 L grade stainless steel using a 100 W nanosecond pulsed fiber laser. The study starts by using single-line machining to study the effect of pulse duration, pulse repetition frequency, and energy dose on the volume of groove and burr formation during engraving. Based on the results from the single line machining, a phenomenological model is proposed to streamline process parameters for area engraving. A correlation is established between the results from the single-line machining and area engraving. The paper concludes by demonstrating that with optimized process parameters, high throughput at high-quality engraving is achievable.

2. Methodology

2.1. Material

316 L grade stainless steel plates with dimensions of 80 mm × 50 mm × 1.5 mm were used. The initial value of average surface roughness (S_a) was measured to be 640 nm using a 3D surface profilometer (Alicona IFM G4) across a field view of 1.43 mm × 1.08 mm. Before engraving, the samples were cleaned with acetone to remove any surface contamination.

2.2. Laser Set-Up

The laser used was an SPI pulsed fiber laser EP-Z G4 with measured average power (P_{av}) of 108 W, a wavelength of 1062 nm, maximum pulse energy of 1.1 mJ, pulse repetition frequency (PRF) up to 1 MHz, a near-Gaussian spatial profile with beam quality (M^2) ≤ 1.6, and pulse duration (τ) in the range 17 to 500 ns termed as waveforms (WFM). Each WFM has a unique PRF (called PRF_0) at which the maximum pulse energy (E_p) and P_{av} are obtained. The measured temporal profile of these waveforms is characterized by a fast rise time peak and a tail portion as shown in Figure 1. The peak offers high peak power which overcomes surface reflectivity and facilitates laser absorption.

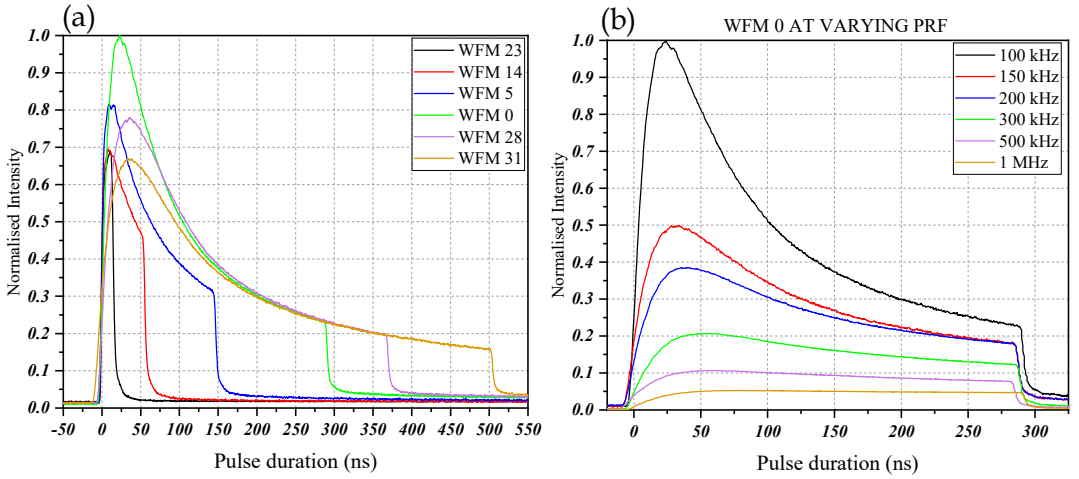

Figure 1. (**a**) Measured temporal profiles of some selected waveforms shortlisted for the experimental work. WFM 23 (17 ns), WFM 14 (60 ns), WFM 5 (150 ns), WFM 0 (280 ns), WFM 28 (380 ns), and WFM 31 (500 ns). (**b**) Temporal profile as a function of pulse repetition frequency (PRF) for WFM 0.

For the laser machining set-up, an optical fiber delivers the laser beam to a collimator, a Raylase® galvanometer scan head (RLA-1504 [Y] D2), and then a 160 mm focal length fused silica f-theta lens that focused the laser beam onto the workpiece. The laser and the galvoscanner are synchronized using a SCAPS® hardware controller and SAMLight 2D® software. The diameter of the collimated beam is 8 mm, providing a focused spot diameter ($2\omega_o$) of 38 µm (calculated at $1/e^2$ of its peak intensity) on the workpiece.

2.3. Experimental Protocol

The experimental approach is summarized in Figure 2, in which a single line machining experiment is used to down-select a suitable range of laser parameters for testing a square-shaped area engraving. The temporal profiles of selected pulse durations (waveforms) are shown in Figure 1a.

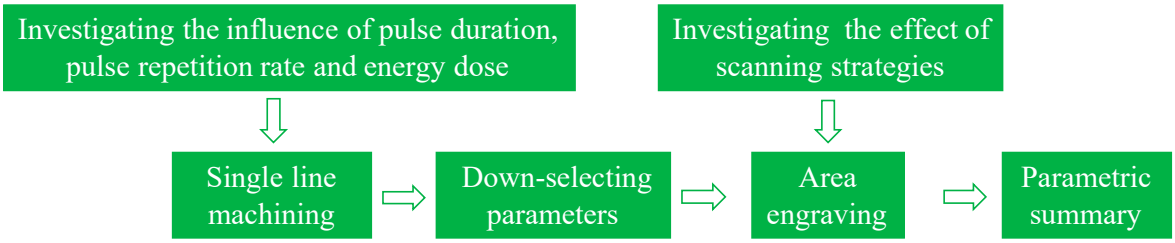

Figure 2. Flowchart of the experimental protocol.

2.3.1. Single Line Machining

Parallel grooves of length 10 mm were machined into the metal workpiece surface, as illustrated in Figure 3a, using the laser process parameters listed in Table 1. The line energy dose (ED_L) is calculated using the formula

$$ED_L = (1\text{mm}/\Delta S) \times E_p, \quad (1)$$

where E_p is the pulse energy and ΔS is the pulse to pulse distance in the scan direction (see Figure 4).

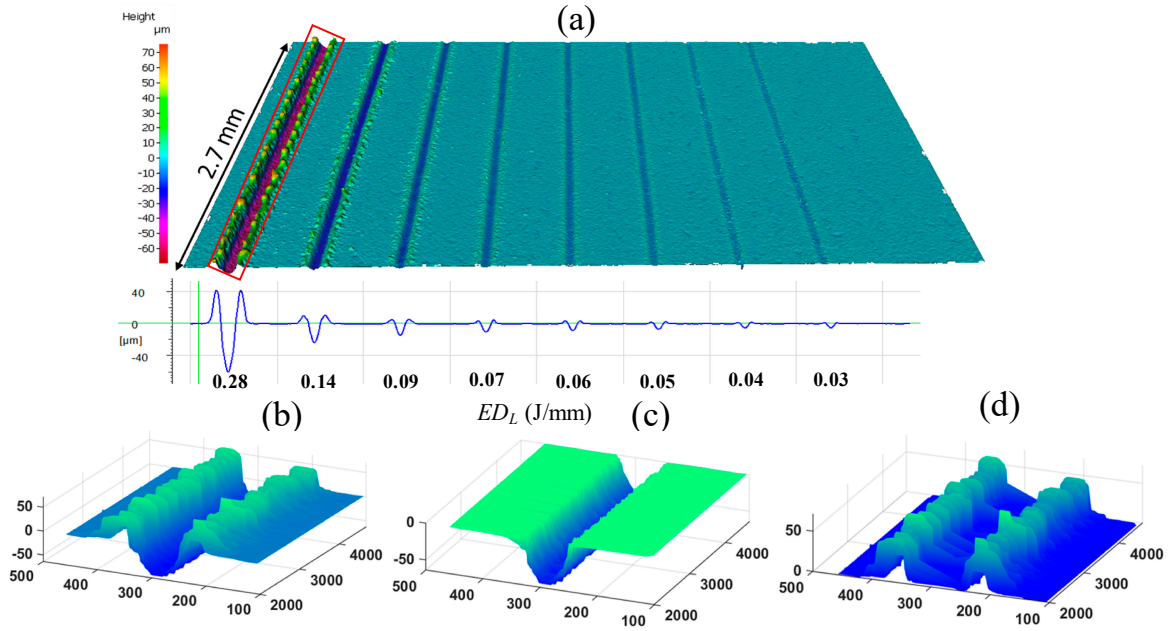

Figure 3. (**a**) Surface height map of lines machined with 280 ns pulses at different line energy doses (ED_L). (**b**–**d**) Extracted 3D profiles of the highlighted region: (**b**) full profile, (**c**) extracted groove profile (material removed), and (**d**) extracted burr profile (redeposited material) [µm].

Table 1. List of parameters for single-line machining study. The pulse to pulse distance (ΔS) and the pulse overlap factor (Po), which is the fraction of the laser spot diameter that overlaps with the previous pulse on the surface of the material, at given energy doses (ED_L) for different pulse durations (τ) are provided. All pulse repetition frequencies (PRF) indicated correspond to the PRF0 condition.

Scan Speed (mm/s)	ED_L **(J/mm)**	**τ, PRF_0, E_p**					
		17 ns 1000 kHz 0.11 mJ	**60 ns 340 kHz 0.32 mJ**	**150 ns 175 kHz 0.62 mJ**	**280 ns 100 kHz 1.1 mJ**	**380 ns 100 kHz 1.1 mJ**	**500 ns 100 kHz 1.1 mJ**
379	0.28	ΔS = 0.4 µm Po = 99%	ΔS = 1.1 µm Po = 97%	ΔS = 2.2 µm Po = 94%	ΔS = 3.8 µm Po = 90%	ΔS = 3.8 µm Po = 90%	ΔS = 3.8 µm Po = 90%
759	0.14	ΔS = 0.8 µm Po = 98%	ΔS = 2.2 µm Po = 94%	ΔS = 4.3 µm Po = 89%	ΔS = 7.6 µm Po = 80%	ΔS = 7.6 µm Po = 80%	ΔS = 7.6 µm Po = 80%
1140	0.09	ΔS = 1.1 µm Po = 97%	ΔS = 3.4 µm Po = 91%	ΔS = 6.5 µm Po = 82%	ΔS = 11.4 µm Po = 70%	ΔS = 11.4 µm Po = 70%	ΔS = 11.4 µm Po = 70%
1520	0.07	ΔS = 1.5 µm Po = 96%	ΔS = 4.5 µm Po = 88%	ΔS = 8.7 µm Po = 77%	ΔS = 15.2 µm Po = 60%	ΔS = 15.2 µm Po = 60%	ΔS = 15.2 µm Po = 60%
1900	0.06	ΔS = 1.9 µm Po = 95%	ΔS = 5.6 µm Po = 85%	ΔS = 10.9 µm Po = 71%	ΔS = 19 µm Po = 50%	ΔS = 19 µm Po = 50%	ΔS = 19 µm Po = 50%
2280	0.05	ΔS = 2.3 µm Po = 94%	ΔS = 6.7 µm Po = 82%	ΔS = 13.0 µm Po = 66%	ΔS = 22.8 µm Po = 40%	ΔS = 22.8 µm Po = 40%	ΔS = 22.8 µm Po = 40%
3000	0.04	ΔS = 3.0 µm Po = 92%	ΔS = 8.8 µm Po = 77%	ΔS = 17.1 µm Po = 55%	ΔS = 30 µm Po = 21%	ΔS = 30 µm Po = 21%	ΔS = 30 µm Po = 21%
3420	0.03	ΔS = 3.4 µm Po = 91%	ΔS = 10.1 µm Po = 74%	ΔS = 19.5 µm Po = 49%	ΔS = 34.2 µm Po = 10%	ΔS = 34.2 µm Po = 10%	ΔS = 34.2 µm Po = 10%

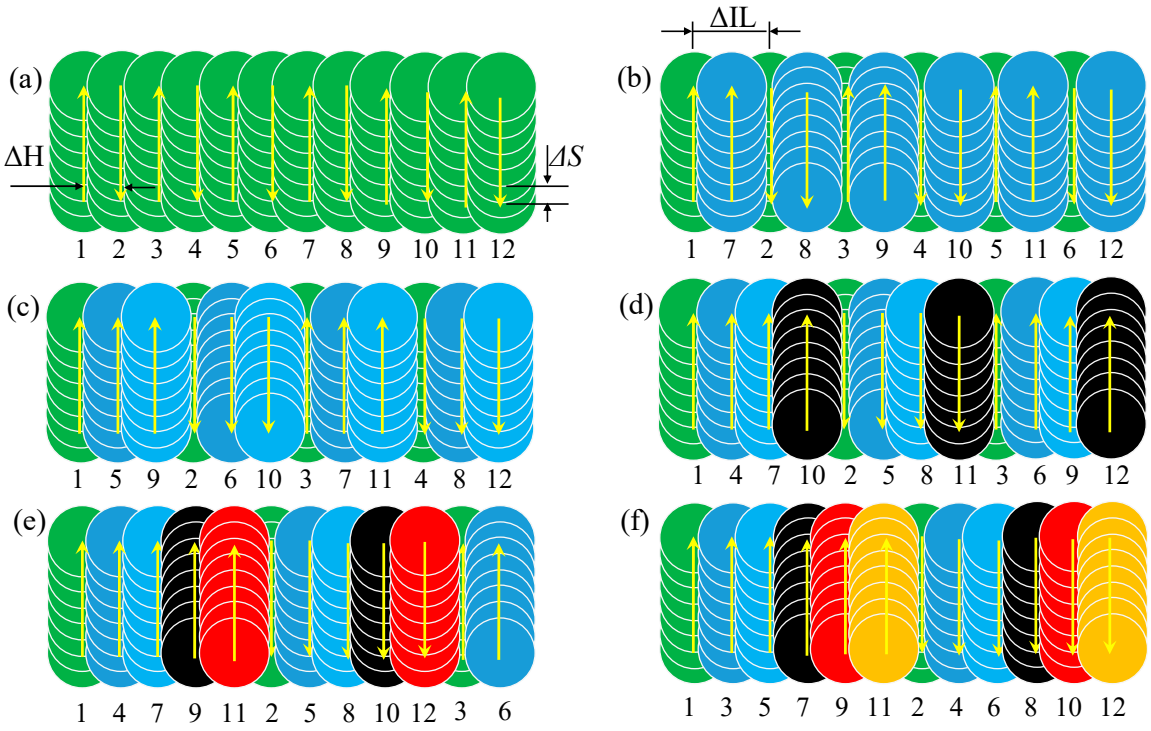

Figure 4. Schematic representation of (**a**) bidirectional sequential method (SM) and (**b**–**f**) bidirectional interlacing method (IM). (**b**) IM with one line skip (ΔIL = 2 Δ*H*), (**c**) IM with 2 line skips (ΔIL = 3 Δ*H*), (**d**) IM with 3 line skips (ΔIL = 4 Δ*H*), (**e**) IM with 4 line skips (ΔIL = 4 Δ*H*), and (**f**) IM with 5 line skips (ΔIL = 5 Δ*H*). In all these scanning modes, the total process time is identical. For image clarity, the hatch distance was chosen at half the laser spot diameter in this illustration.

For this study, the effect of ED_L and τ on the volume of groove and burr formation was investigated. Using the parameters listed in Table 2, the influence of changing PRF at a constant ED_L was examined. Each parameter combination was replicated three times and the mean value presented.

Table 2. List of parameters for investigating the influence of PRF on single-line machining at a scan speed of 1140 mm/s (ED_L = 0.09 J/mm).

PRF (kHz)	E_p (mJ)	Po (%) at 0.09 J/mm
100	1.08	70
150	0.72	80
200	0.54	85
250	0.43	88
300	0.36	90
350	0.31	91
400	0.25	93

2.3.2. Area Machining Experiment

Following the single-line machining study, square-shaped area machining was investigated, in each case based on the machining of a 5 × 5 mm^2 flat-bottomed area using a parallel hatch distance (Δ*H*) of 13.3 µm, which was chosen out of several hatch distances to give the highest MRR and better S_a. The corresponding area energy dose (ED_A) from the down-selected parameters was calculated as follows.

$$ED_A = (1\text{mm}/\Delta H) \times ED_L, \quad (2)$$

An initial study was conducted to investigate the influence of laser beam scanning strategies on MRR and S_a using SM and IM, as shown schematically in Figure 4. In these experiments, the interlacing

distance (ΔIL) was varied at 13.3 µm, 26.6 µm, 39.9 µm, 53.2 µm, 66.5 µm. and 79.8 µm to identify an optimized value for further studies. More details of this method of machining are presented in our previous work [19].

To prevent a possible Moiré effect, the laser scanning angle was changed after each full machining pass, to give four different angles (0°, 45°, 18.43°, and 71.58°), popularly known as "halftone angles". Gora et al. studied the effect of scanning patterns during laser polishing [21]. They found that a better surface finish was achievable by using the halftone angles. The total number of passes during the area engraving test was 20. Finally, in a similar way as the single-line machine experiment, the influence of τ and PRF at constant ED_A was investigated.

2.4. Sample Postprocessing and Analysis

The processed samples were cleaned with deionized water in an ultrasonic bath at 25 °C for 10 min to remove loose particles. To avoid possible end effects, only the central section of the grooves at a sampling length (L) of 2.7 mm was measured. A 3D-profile of each groove was obtained using the Alicona surface profilometer. Using a MATLAB™ script, the profile of each machined line was processed (see Figure 3b) and separated into the groove (material removed) (see Figure 3c) and the burr (redeposited material) (see Figure 3d). During the groove analysis, the sample was levelled so that the data above and below the levelled surface were used to calculate the area of burr and groove respectively using Equation (3). The volume of groove and burr are calculated using Equation (4).

$$A = \iint_{x,y} z(x,y).dx.dy, \tag{3}$$

$$V = A \times L, \tag{4}$$

After the 3D profiling, each groove was sectioned in the middle, cold mounted, polished, and then examined using a Leica optical microscope (DM6000M) at × 20 magnification (see Figure 5b). For the area machining experiment, a 3D profile was obtained for each parameter combination and, from this, the depth was determined and subsequently used to calculate an overall MRR value (the product of the depth and area of engraving per unit processing time). The arithmetic average of absolute surface roughness (S_a) was obtained using a cut-off wavelength of 284 µm.

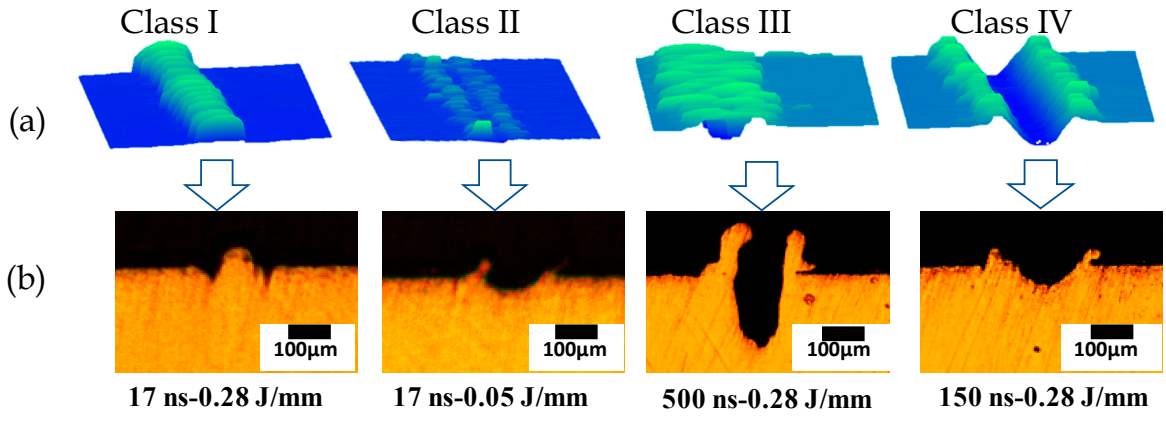

Figure 5. (**a**) 3D profiles of various classes of groove produced during the single-line machining and the (**b**) corresponding cross-sectional profiles.

3. Results and Discussion

3.1. Single Line Machining Experiment

3.1.1. Groove Analysis

In general, four classes of grooves were observed as shown in Figure 5. Class I is representative of closed-up grooves which result from a combination of high ED_L (0.28 J/mm) and high Po (99%). Class II is representative of shallow grooves resulting from lower ED_L and τ, in this case, 0.05 J/mm at 17 ns. In Class III, there is a pronounced burr formation at the edges of the groove, which suggests an inefficient removal of molten material. In extreme conditions, this can result in a Class I groove. The nature of this type of groove obstructs proper surface profiling (see Class III Figure 5a).

Class IV represents a stable groove with a well-defined groove and burr which represents a condition suitable for analysis. Based on the above classifications, the 17 ns pulses with an ED_L of 0.28 J/mm and any ED_L below 0.05 J/mm were eliminated from the parametric analysis in the section below. The general classification of grooves as elaborated above corroborates results presented by (Leone et al., 2018). Their study investigated parametric influence during laser marking application of Inconel 718 using a 30 W Q-switched Yb: YAG fiber laser.

3.1.2. Influence of Change in ED_L and τ on Groove and Burr Formation

As expected, an increase in ED_L increases both the volume of the groove and that of the burr, as shown in Figure 6. When a keyhole is produced as a result of high ED_L, the depth increases such that subsequent ejection due to the recoil pressure is compromised. This leads to an ineffective ejection and excessive burr formation, as shown in the highlighted region in Figure 6c, in some cases collapsing back into the machined region (see the results for τ = 60 ns at ED_L = 0.28 J/mm). The evidence presented does not suggest that material removal is solely through melt ejection, in fact, some material is removed through vaporization; however, the method used cannot quantify this effect.

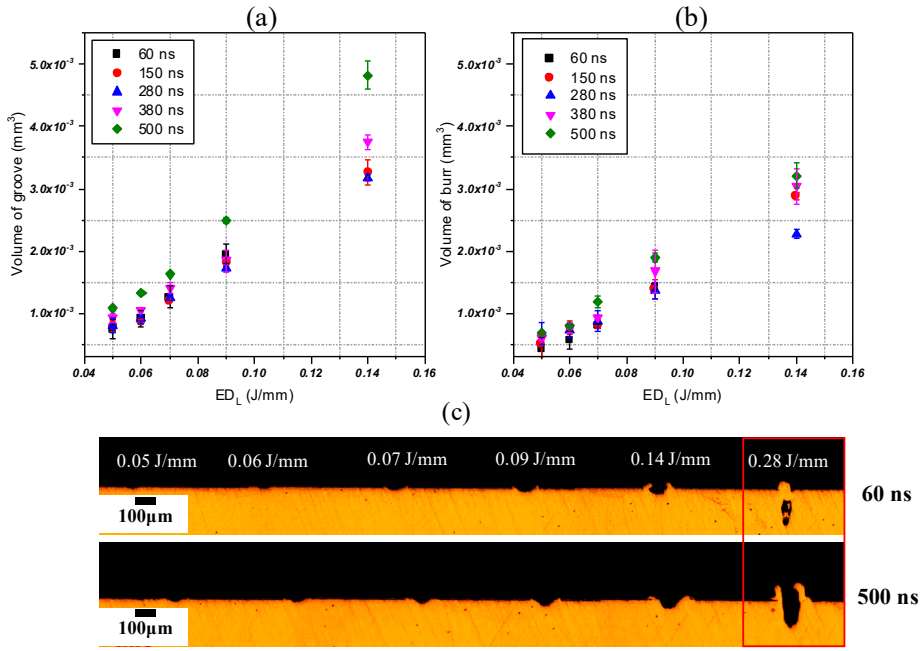

Figure 6. (**a**) Extracted volume of groove and (**b**) extracted volume of burr produced as a function of line energy dose (ED_L) for different pulse durations at PRF_0. (**c**) Cross section of grooves produced at 60 ns and 500 ns pulse durations for different energy doses. The parameter combinations highlighted in red have been excluded from further experiments as the quality of machining is poor.

As shown in Figure 6a, longer τ produces larger grooves, as is particularly evident at 380 ns and 500 ns for the highest ED_L. This is likely due to more laser interaction time and deeper thermal penetration at longer τ. This is influenced by the extended intensity distribution profile as presented in Figure 1, which helps retain heat before successive pulses. The similar volume of the groove at 60 ns, 150 ns, and 280 ns τ at lower ED_L is attributable to the high pulse overlap as detailed in Table 1. From Figure 6b,c, although longer τ typically leads to a higher burr volume, a shorter τ with high pulse overlap inhibits rapid heat dissipation resulting in heat accumulation, which increases the burr volume. From the above observations, it seems likely that a longer τ will give a high MRR with higher S_a at higher ED_L during area engraving due to the high melt and burr formation. Shorter τ, such as 60 ns and 150 ns, with high ED_L may as well result in higher MRR, but this might be at the expense of surface quality.

3.1.3. Effect of Change in PRF and τ on the Volume of Groove and Burr Formation

Given the requirement for high MRR, τs of 280 ns, 380 ns, and 500 ns were selected for further investigation, to evaluate the impact of PRF. Here, the ED_L was kept constant at 0.09 J/mm as this provided a good combination of high MRR and machining quality. Results in Figure 7 indicate that an increase in PRF increases the volume of both groove and burr. However, a critical point is reached where the groove collapses.

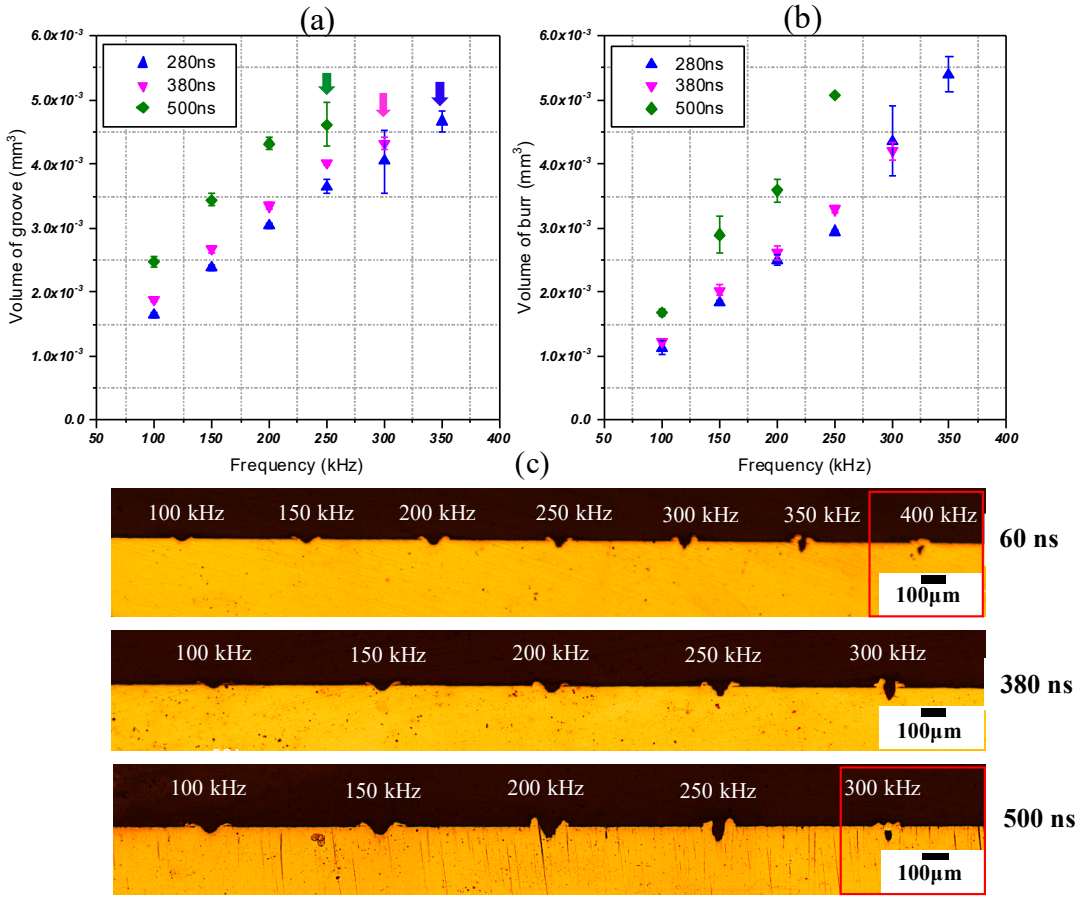

Figure 7. (**a**) Volume of groove; (**b**) volume of the burr as a function of PRF at a constant ED_L of 0.09 J/mm; and (**c**) cross-sectional view for the influence of change in PRFs at 280 ns, 380 ns, and 500 ns.

This happens at a PRF above 250 kHz at 500 ns, 300 kHz at 380 ns, and 350 kHz at 280 ns (see arrowed points on Figure 7a). An increase in τ increases the volume of groove and burr formation for similar reasons to those earlier discussed. The increased volume of groove and burr at higher ED_L or

higher PRFs is assumed to result from the thermal accumulation and the consequent larger melt zone. However, the reduction in E_p and the change in temporal profile (Figure 1b) at high PRF decreases the pulse intensity and this lowers the vapor pressure needed for effective removal, as seen in the highlighted areas of Figure 7c. The critical PRF (PRF beyond which groove is unstable) is dependent on τ due to the differences in laser interaction time. The higher laser-material interaction time for longer τ means more melt, however, due to the reduction in E_p at high PRF (less energetic pulse), the melt collapses (see Figure 7c—500 ns at 300 kHz) and therefore lowers the critical PRF.

In general, it can be hypothesized that higher PRF and higher ED_L would cause high MRR, but the increase in the volume of burr could imply a higher S_a during area engraving. Finally, it can be suggested that the closing of shallow grooves at high PRFs could provide a polishing effect. Based on the results above, a phenomenological model is proposed such that the full parametric range indicated in Tables 1 and 2 were down-selected by excluding pulse duration 17 ns, $ED_L > 0.09$ J/mm, $ED_L < 0.04$ J/mm, and PRF of 400 kHz. The corresponding ED_A values from these down-selected parameters were used to investigate the transferability of results from the single-line machining to a square-shaped area engraving.

3.2. Area Machining Experiment

3.2.1. Effect of Different Laser Beam Scanning Strategies

In Figure 8, the SM Figure 8b is compared with different IMs (Figure 8c–g) for a mid-range ED_A of 4.2 J/mm^2 (ED_L = 0.06 J/mm and ΔH = 13.3 µm) processed at 280 ns. A blackened surface and higher burr formation at the edges were observed with SM (see Figure 8a).

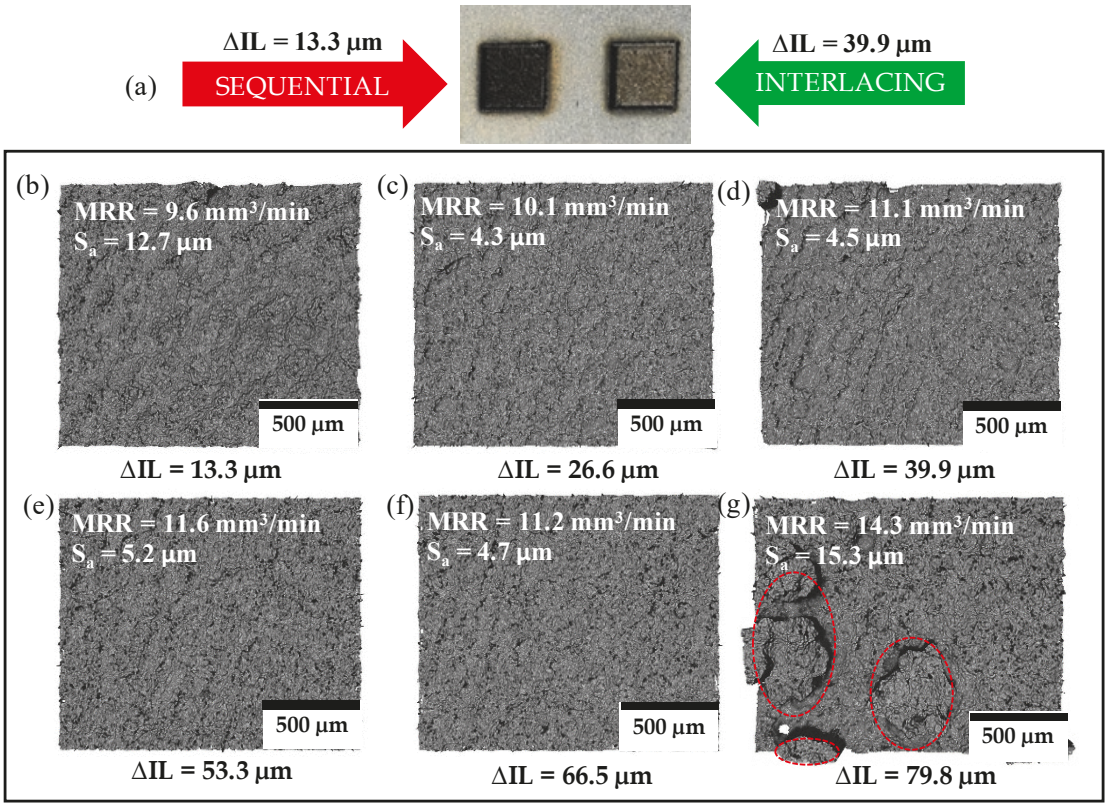

Figure 8. (**a**) Photograph comparing sequential method (SM) to interlacing method (IM). (**b**) Surface morphology for SM. (**c**–**g**) Surface morphology at different interlacing distances (ΔIL), produced at a scan speed of 1900 mm/s, 280 ns and ED_A= 4.2 J/mm^2.

The S_a is reduced by a factor of 3 and the MRR is increased by 20% with IM (see Figure 8c–f). Figure 9 presents the cross-sectional differences between IM and SM at ED_A = 5.3 J/mm^2. At higher ED_A, IM significantly reduces the S_a by 84% at a slightly higher MRR. The time delay between adjacent scan for IM helps reduce undue heat accumulation in the workpiece.

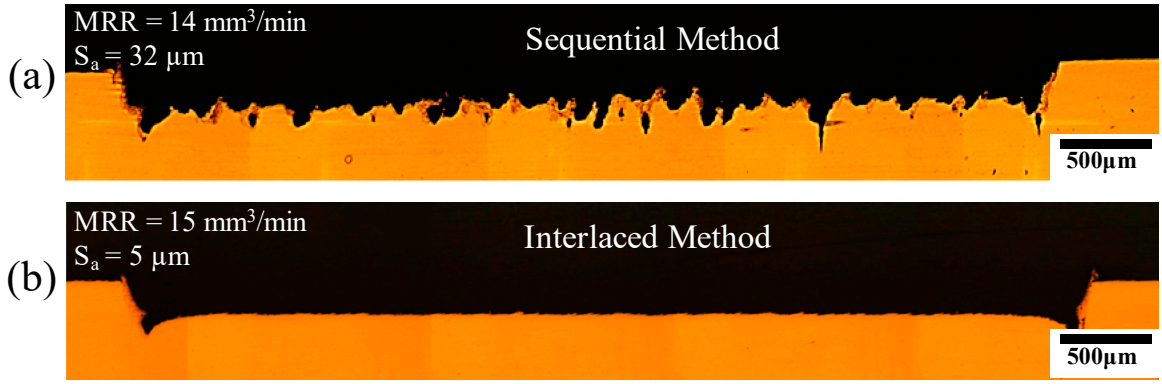

Figure 9. Cross-sectional profile highlighting the difference between (**a**) SM at material removal rate (MRR) = 14 mm^3/min, S_a = 32 µm and (**b**) IM at MRR = 15 mm^3/min, S_a = 5 µm processed at 5.3 J/mm^2 at 280 ns.

This implies a uniform thermal gradient around the processed area which could cause a more efficient cooling. With SM, the heat is built up to produce more melt. The ineffective removal of this melt ends up compromising MRR and S_a. Figure 9 also illustrates the presence of undercut at the corners for both SM and IM, which is due to the lack of synchronization between the laser and the scanner system. This feature compromises the engraving quality; however, with appropriate scan delays this effect can be rectified.

For glass, the authors of [19,22] suggest that the IM increases laser coupling efficiency as a result of the smaller angle of incidence of the laser beam. This results from the perpendicular beam interaction to the surface in the case of IM as opposed to the SM, where the beam is incident on the wall of the previously machined groove. This could as well contribute to the differences observed for both scanning strategies. Although a change in interlacing distance increases MRR, at ΔIL = 79.8 µm (see Figure 8g) the surface quality is deteriorated and characterized by massive structures (solidified melt redeposition) resulting from ineffective melt ejection. Obviously, IM offers a better surface quality in comparison to SM, hence all results presented below in the next sections were conducted using IM at an optimized ΔIL of 39.9 µm (see Figure 8d) due to its high MRR and low S_a.

3.2.2. Influence of Change in ED_A and τ on the MRR and S_a

As shown in Figure 10, an increase in ED_A and τ leads to a general increase in both MRR and S_a, as suggested in Section 3.1.2. From Figure 10b, there is a critical ED_A at 5.3 J/mm^2 for 60 ns, 150 ns, and 500 ns (see the dashed line) where the S_a starts to reduce for further increase in ED_A, which is most likely attributable to the "closing-up" effect observed in the single-line machining experiments, rather than any inherent machining quality improvement. The shorter τ gives lower MRR coupled with high S_a values mainly due to the high pulse overlaps employed in this study (see Table 1). An increase in scan speed could offset the issues of high overlap, but this would mean a lower MRR which is not consistent with the overall requirement for high throughput engraving. This highlights the trade-off between high-throughput and high-quality engraving, and, therefore, to maintain a balance, the area highlighted in green in Figure 10 with MRR in the range of 5 to 16 mm^3/min and corresponding S_a of 2.6–13 µm is an area of focus for high-quality engraving.

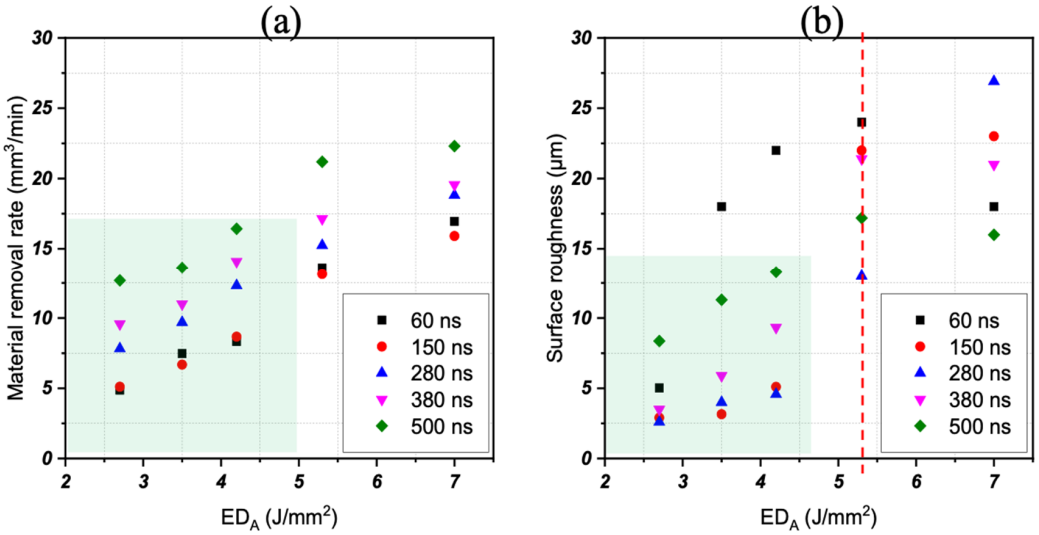

Figure 10. (**a**) MRR and (**b**) S_a as a function of area energy dose (ED_A) for different pulse durations. The highlighted region in panel (**a**) excludes 60 ns (>2.7 J/mm^2), and the dashed line represents a critical ED_A beyond which the surface is blackened and surface quality deteriorates significantly.

Clearly, to achieve S_a below 2.6 µm at high MRR, it is recommended to use a sequential combination of deep engraving with longer pulse durations (>280 ns) and periodic cleaning with shorter pulses (<280 ns) at lower ED_A (<2.7 J/mm^2). The increase in MRR as a function of τ agrees with previous work on the use of 20 W nanosecond pulsed fiber laser engraving of stainless steel by Manninen et al [23].

3.2.3. Influence of Change in PRF and τ on the MRR and S_a

Considering ED_A at 4.2 J/mm^2 for longer τ (>150 ns), the influence of PRF was investigated. As demonstrated in Figure 11a, increasing PRF results in an initial increase in MRR up to a critical PRF value (200 kHz for 380 ns and 280 ns) after which the MRR starts to decline. As discussed earlier, thermal accumulation plays a key role in the increase in MRR at an increased PRF, but, as the MRR increases, so does the surface roughness, as seen in Figure 11b.

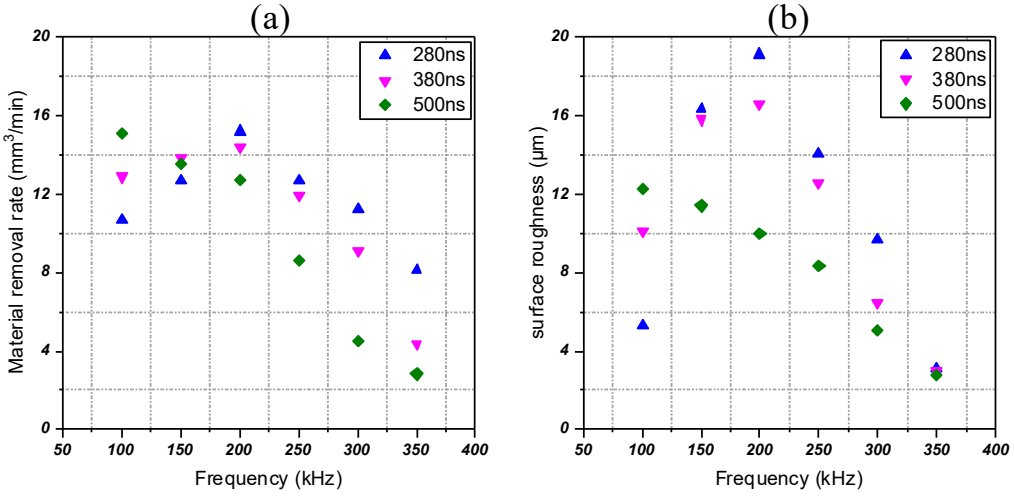

Figure 11. (**a**) MRR and (**b**) S_a as a function of PRF and τ at a constant ED_A of 4.2 J/mm^2.

As more melt is formed, the impact from subsequent pulses ejects melt across the surface, and rapid solidification of this splashed melt results in high S_a values. Beyond the critical PRF, the S_a drops due to a reduction in pulse energy at higher PRFs. Interestingly, 500 ns show a general reduction in MRR and S_a as PRF increases. This phenomenon was partially observed during the single-line machining

experiment where the groove close-up effect occurred earlier for 500 ns which could be as a result of the longer laser interaction time and lower laser intensity at higher PRFs.

Figures 12 and 13 show scanning electron microscope (SEM) micrographs of the surfaces processed at 4.2 J/mm^2 with 280 ns and 500 ns pulse durations, respectively, distinguishing between the surface morphology for 280 ns and 500 ns at various PRFs. Typical surface features are highlighted, created by the intensity of the laser pulse and the mechanisms of melt flow and surface tension. Wu et al. conducted a similar experiment to investigate the impact of a change in PRF on surface morphology using a picosecond laser for machining Cr12MoV cold work mold steel [5]. The study highlighted the impact of heat accumulation at higher PRFs and also reported an improved surface quality at higher PRFs which agrees with the results presented here. The paper, however, did not provide the typical MRR achieved at such high PRFs.

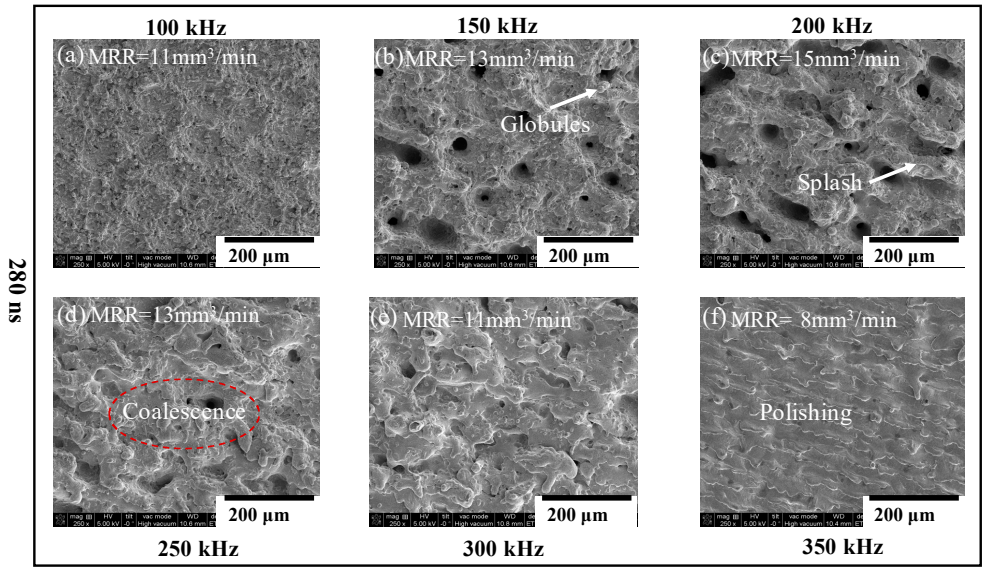

Figure 12. SEM micrographs of the surface topology at different PRFs processed at ED_A of 4.2 J/mm^2 at 280 ns.

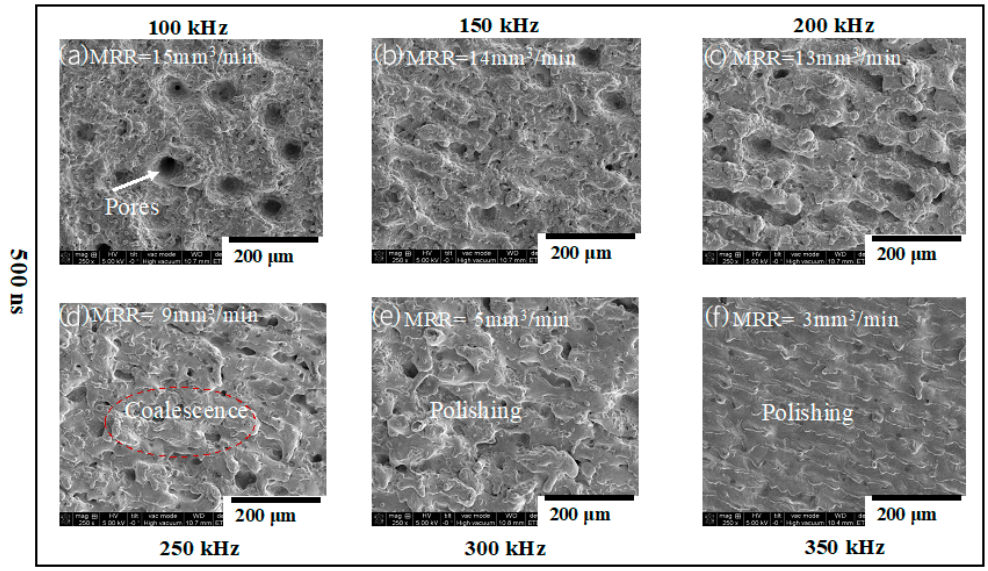

Figure 13. SEM micrographs of the surface morphology processed at different PRFs at ED_A of 4.2 J/mm^2 at 500 ns.

For the 280 ns sequence (see Figure 12), the good surface quality at low PRF (100 kHz) is due to efficient ejection, whereas the middle frequencies show evidence of unstable and partial ejection. At the highest PRF, the S_a begins to improve again, but this is associated with a less energetic melt resulting from a reduction in pulse energy, as further evidenced by the associated reduction in MRR (see Figure 12f). The coalescence of melt which represents a smoothing effect is more pronounced for 500 ns (see Figure 13f) and therefore would serve as a better parameter for laser polishing. Vadali et al. reported a similar result where longer τ were deemed capable of attenuating longer wavelengths and hence results in better S_a [24]. This was presented in a study they conducted to investigate the influence of τ on the laser polishing of Ti6Al4V.

Even though the single-line machining approach did not take into consideration multiple passes, it predicts the parametric influence on MRR and S_a during area engraving. It, therefore, serves as a quick model to shortlist parameters for a multi-pass area engraving.

4. High-Quality Engraving

As suggested in Section 3.2.2, an engraving strategy has been adapted using three different parametric combinations: (i) deep engraving with longer τ at high ED_A, (ii) periodic cleaning passes using shorter τ at low ED_A, and (iii) final polishing using longer τ at higher PRF. Figure 14 depicts two engraved structures: (a) a square of constant depth with MRR of 13 mm^3/min providing S_a ~1.4 µm and (b) an inverted stepped pyramidal structure using similar engraving parameters in (a) while compensating for the change in depth at each stage during the engraving.

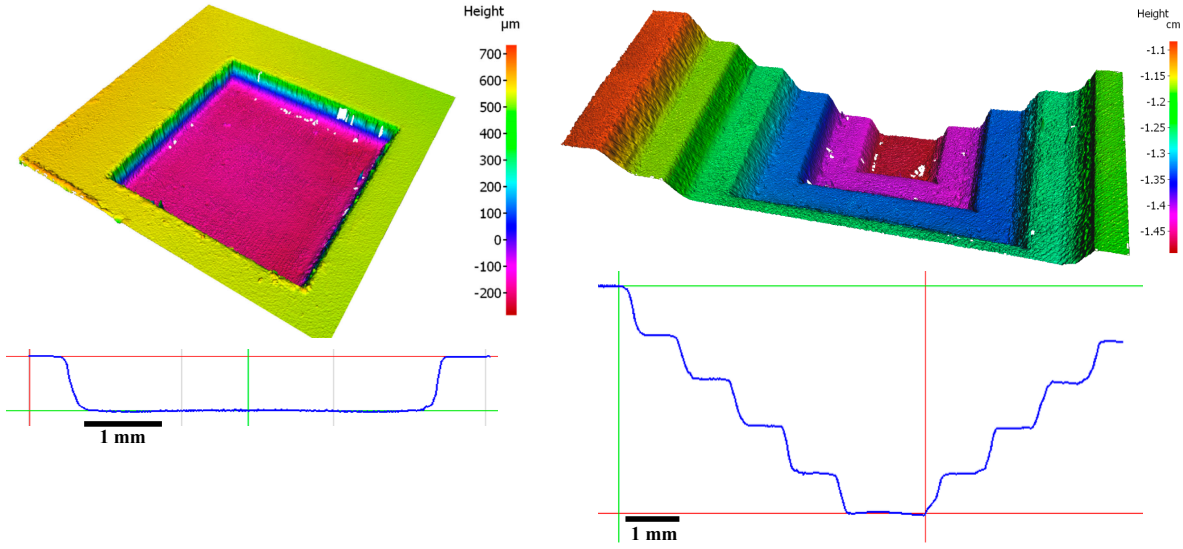

Figure 14. Morphology of high-quality constant depth area engraving (**a**) 13 mm^3/min MRR at 1.4 µm S_a using: Engraving pass at 4.2 J/mm^2, 380 ns, 175 kHz; Cleaning pass at 150 ns, 350 kHz, 3.5 J/mm^2 and polishing pass at 1.82 J/mm^2, 500 ns, 500 kHz using IM and halftone scanning. (**b**) Inverted stepped pyramid-shaped engraving.

5. Conclusions

A systematic experimental approach has been used to investigate 100 W nanosecond pulsed fiber laser engraving of 316L grade stainless steel. The study sought to optimize process parameters for high-quality area engraving using a simple single-line machining technique while investigating the influence of laser beam scanning strategies. A significant finding to emerge from this study is that an IM laser beam scanning strategy reduces undue heat accumulation and serves as a better option to the traditional SM. We report that IM not only provide a lower S_a, but also increases MRR. Again, a change in the interlacing distance increases MRR at considerably lower S_a; however, beyond a critical value, the S_a deteriorates. The study also established that a combination of longer τ, higher ED_A, and PRF

slightly above the PRF_0 produces a high MRR at high S_a. However, at higher PRF, there is a change in the engraving mechanism which initiates a polishing effect. For low S_a and MRR, a shorter τ at low ED_A is required.

Overall, we have shown that high-quality engraving is possible for high power engraving only when IM is coupled with careful parametric combinations. A further study would be a thermal analysis and surface elemental compositional change for both SM and IM. It will also be interesting to investigate the impact of IM on other metals to explore its full potential and finally, consolidate the findings to produce high-quality engraving.

Author Contributions: S.D.D.: Conceptualisation, Methodology, Investigation, Visualisation, Writing-original draft. K.L.W.: Supervision, Writing—review and editing. P.H.: Supervision, Writing—review and editing. A.R.: Supervision, Writing—review and editing. J.G.: Funding acquisition, Resources. R.L.R.: Supervision, Writing—review and editing. D.P.H.: Resources, Supervision, Writing—review and editing. All authors have read and agreed to the published version of the manuscript.

Funding: This research received no external funding.

Conflicts of Interest: The authors declare no conflict of interest.

References

1. Lopez, J.; Zaouter, Y.; Torres, R.; Faucon, M.; Hönninger, C.; Georges, P.; Kling, R. Parameters of influence in surface ablation of metals with using a high power tunable ultrafast laser. In Proceedings of the ICALEO 2013—32nd International Congress on Applications of Lasers and Electro-Optics, Miami, FL, USA, 6–10 October 2013.
2. Lopez, J.; Mishchik, K.; Mincuzzi, G.; Audouard, E.; Mottay, E.; Kling, R. Efficient Metal Processing Using High Average Power Ultrafast Laser. *J. Laser Micro/Nanoeng.* **2017**, *12*, 296–303. [CrossRef]
3. Knowles, M.R.H.; Rutterford, G.; Karnakis, D.; Ferguson, A. Micro-machining of metals, ceramics and polymers using nanosecond lasers. *Int. J. Adv. Manuf. Technol.* **2007**, *33*, 95–102. [CrossRef]
4. Genna, S.; Leone, C.; Lopresto, V.; Santo, L.; Trovalusci, F. Study of fibre laser machining of C45 steel: Influence of process parameters on material removal rate and roughness. *Int. J. Mater. Form.* **2010**, *3* (Suppl. 1), 1115–1118. [CrossRef]
5. Wu, B.; Deng, L.; Liu, P.; Zhang, F.; Duan, J.; Zeng, X. Effects of picosecond laser repetition rate on ablation of Cr12MoV cold work mold steel. *Appl. Surf. Sci.* **2017**, *409*, 403–412. [CrossRef]
6. Petkov, P.V.; Dimov, S.S.; Minev, R.M.; Pham, D.T. Laser milling: Pulse duration effects on surface integrity. *Proc. Inst. Mech. Eng. Part B J. Eng. Manuf.* **2008**, *222*, 35–45. [CrossRef]
7. Anisimov, S.I.; Luk'yanchuk, B.S. Selected problems of laser ablation theory. *Physics-Uspekhi* **2002**, *45*, 293–324. [CrossRef]
8. Shi, W.; Zhang, Q. High power nanosecond pulsed fiber lasers and applications. In Proceedings of the 2014 IEEE Photonics Conference, IPC 2014, San Diego, CA, USA, 12–16 October 2014; Volume 3, pp. 392–393. [CrossRef]
9. Su, R.; Zhou, P.; Xiao, H.; Wang, X.; Xu, X. 150 W high-average-power, single-frequency nanosecond fiber laser in strictly all-fiber format. *Appl. Opt.* **2012**, *51*, 3655–3659. [CrossRef] [PubMed]
10. Limpert, J.; Höfer, S.; Liem, A.; Zellmer, H.; Tünnermann, A.; Knoke, S.; Voelckel, H. 100-W Average-Power, High-Energy Nanosecond Fiber Amplifier. *Appl. Phys. B.* **2002**, *75*, 477–479. [CrossRef]
11. Lopez, J.; Mincuzzi, G.; Devillard, R.; Zaouter, Y.; Hönninger, C.; Mottay, E.; Kling, R. Ablation efficiency of high average power ultrafast laser. *J. Laser Appl.* **2015**, *27*, S28008. [CrossRef]
12. Schille, J.; Schneider, L.; Loeschner, U. Process optimization in high-average-power ultrashort pulse laser microfabrication: How laser process parameters influence efficiency, throughput and quality. *Appl. Phys. A* **2015**, *120*, 847–855. [CrossRef]
13. Raciukaitis, G.; Brikas, M.; Gecys, P.; Gedvilas, M. Accumulation effects in laser ablation of metals with high-repetition-rate lasers. In Proceedings of the Volume 7005, High-Power Laser Ablation VII 2008, Taos, NM, USA, 20–24 April 2008; p. 70052. [CrossRef]

14. Neuenschwander, B.; Jaeggi, B.; Zimmermannn, M.; Markovic, V.; Resan, B.; Weingarten, K.; Penning, L. Laser surface structuring with 100 W of average power and sub-ps pulses. *J. Laser Appl.* **2016**, *28*, 022506. [CrossRef]
15. Deladurantaye, P.; Gay, D.; Cournoyer, A.; Roy, V.; Labranche, B.; Levesque, M.; Taillon, Y. Material micromachining using a pulsed fiber laser platform with fine temporal nanosecond pulse shaping capability. In Proceedings of the SPIE Fiber Lasers VI: Technology, Systems, and Applications, San Jose, CA, USA, 26–29 January 2009; Volume 7195, p. 71951S. [CrossRef]
16. Schille, J.; Schneider, L.; Streek, A.; Kloetzer, S.; Loeschner, U. High-throughput machining using a high-average power ultrashort pulse laser and high-speed polygon scanner. *Opt. Eng.* **2016**, *55*, 096109. [CrossRef]
17. Raciukaitis, G. Use of High Repetition Rate and High Power Lasers in Microfabrication: How to Keep the Efficiency High? *J. Laser Micro/Nanoeng.* **2009**, *4*, 186–191. [CrossRef]
18. Leone, C.; Bassoli, E.; Genna, S.; Gatto, A. Experimental investigation and optimisation of laser direct part marking of Inconel 718. *Opt. Lasers Eng.* **2018**, *111*, 154–166. [CrossRef]
19. Wlodarczyk, K.; Lopes, A.; Blair, P.; Maroto-Valer, M.M.; Hand, D.P. Interlaced Laser Beam Scanning: A Method Enabling an Increase in the Throughput of Ultrafast Laser Machining of Borosilicate Glass. *J. Manuf. Mater. Process.* **2019**, *3*, 14. [CrossRef]
20. Gora, W.S.; Tian, Y.; Cabo, A.P.; Ardron, M.; Maier, R.R.J.; Prangnell, P.; Hand, D.P. Enhancing surface finish of additively manufactured titanium and cobalt chrome elements using laser based finishing. *Phys. Procedia* **2016**, *83*, 258–263. [CrossRef]
21. Malinowski, A.; Gorman, P.; Codemard, C.A.; Ghiringhelli, F.; Boyland, A.J.; Marshall, A.; Durkin, M.K. High-peak-power, high-energy, high-average-power pulsed fiber laser system with versatile pulse duration and shape. *Opt. Lett.* **2013**, *38*, 4686. [CrossRef] [PubMed]
22. Wlodarczyk, K.L.; Schille, J.; Naumann, L.; Lopes, A.A.; Bitharas, I.; Bidare, P.; Maroto-Valer, M.M. Investigation of an interlaced laser beam scanning method for ultrashort pulse laser micromachining applications. *J. Mater. Process. Technol.* **2020**, *285*, 116807. [CrossRef]
23. Manninen, M.; Hirvimäki, M.; Poutiainen, I.; Salminen, A. Effect of Pulse Length on Engraving Efficiency in Nanosecond Pulsed Laser Engraving of Stainless Steel. *Metall. Mater. Trans. B* **2015**, *46*, 2129–2136. [CrossRef]
24. Vadali, M.; Ma, C.; Duffie, N.A.; Li, X.; Pfefferkorn, F.E. Effects of pulse duration on laser micro polishing. *J. Micro Nano-Manuf.* **2013**, *1*, 291–297. [CrossRef]